Mask-guided Spatial-Temporal Graph Neural Network for Multi-frequency Electrical Impedance Tomography

Mask-guided Spatial-Temporal Graph Neural Network for Multi-frequency Electrical Impedance Tomography

Zhou Chen, *Student Member, IEEE,*, Zhe Liu, *Student Member, IEEE,*, Lulu Ai, Sheng Zhang, and Yunjie Yang, *Member, IEEE*

***Abstract*—Multi-frequency Electrical Impedance Tomography (mfEIT) is an emerging biomedical imaging modality that exploits frequency-dependent electrical properties. The mfEIT-image-reconstruction problem for cell imaging is particularly challenging due to weak signals from miniaturized sensors and high sensitivity to modelling errors. Existing approaches are primarily based on the linearized model and few are applied to the miniaturized setup. Here we report a Mask-guided Spatial-Temporal Graph Neural Network (M-STGNN) to reconstruct mfEIT images in cell culture imaging. The M-STGNN captures simultaneously spatial and frequency correlations, and the spatial correlation is further constrained by geometric structures from auxiliary binary masks, such as CT or microscopic images. We validate the mfEIT approach through numerical simulations and experiments on MCF-7 human breast cancer cell aggregates. The results demonstrate the superiority of M-STGNN over the state of the art with an improvement of approximately 10.7% under the experimental setup. It can be readily extended to multi-modal biomedical imaging applications.**

***Index Terms*—Graph neural network, deep learning, electrical impedance tomography, multi-frequency, image reconstruction.**

I. Introduction

MULTI-FREQUENCY Electrical Impedance Tomography (mfEIT) is a tomographic modality that reconstructs the spectroscopic conductivity images associated with intrinsic tissue properties [1]–[3]. Currents with a sequence of frequencies are injected into the boundary electrodes and induced voltages are acquired to infer the spatial conductivity distribution at given frequencies [4], [5]. mfEIT provides appealing benefits of low-cost fabrication, portability, non-destructiveness, radiation-free measurement and fast imaging speed. As the different electrical characteristics between various tissues can be exploited for physiological and pathological diagnostics, mfEIT has been investigated for diagnostic imaging, such as acute stroke detection [6], [7], cardiac activity imaging [8], breast cancer detection [9], [10], and functional lung imaging [11], [12]. With the development of microtechnologies, mfEIT with miniaturized sensors also shows its potential in tissue engineering at the cellular level by providing label-free and non-destructive imaging and monitoring of cellular dynamics [3], [13], [14]. Yang *et al.* [3] performed 3D imaging of breast cancer cell spheroids in 3D scaffolds. Wu *et al.* [13], [14] demonstrated the use of mfEIT in monitoring cell growth and viability. However, sensor miniaturization [15], [16] makes 3D cell culture imaging challenging due to weak measurement signals and sensitivity to modelling errors. Therefore, enhancing noise robustness and facilitating high-quality mfEIT imaging have become increasingly demanding.

One of the major challenges of mfEIT comes from the nonlinear and severe ill-posed nature of the image reconstruction problem, which requires simultaneous reconstruction of multiple frequency-dependent conductivity distributions. Existing literature commonly addresses the mfEIT-image-reconstruction problem in the linearized regime. Most work reconstructs the image under each frequency independently based on mono-frequency reconstruction algorithms such as GREIT [17], Total Variation (TV) regularization [18], or sparsity regularization [19]. Others approximate the forward model of mfEIT based on the Multiple Measurement Vector (MMV) model [20]. The MMV model constrains the solutions by joint-sparsity to reconstruct multiple conductivity distributions of varying frequencies at the same time. Alberti *et al.* [21] proposed to optimize the MMV model by using Iterative Soft Thresholding (IST) to combine the strengths of IST and Group Sparsity (GS). Alternatively, the MMV model can be optimized by the prevailing Alternating Direction Method of Multipliers (ADMM) that has been applied in multi-frequency complex-valued Electrical Capacitance Tomography (ECT) [22]. In our previous work [23], ADMM was unrolled with a finite number of iterations into a single network to solve the MMV problem. We demonstrated that this unrolling approach can notably improve the image quality by combining the advantages of the MMV model and deep neural network. The mfEIT-image-reconstruction problem can also be interpreted using a Bayesian statistical inversion framework. For instance, Liu *et al.* [24] and Xiang *et al.* [25] addressed the multi-frequency tomographic imaging problem by utilizing the Sparse Bayesian Learning (SBL) framework based on the MMV model. Despite the noteworthy progress, these approaches depend on either the linearized mfEIT model or strong sparsity assumption, which restricts their performance for non-linear or non-sparse situations. Therefore, we in this

Manuscript Received xxx. This work is supported by the Data Driven Innovation Chancellor's Fellowship at The University of Edinburgh.

Z. Chen, Z. Liu and Y. Yang are with the Intelligent Sensing, Analysis and Control Group, Institute for Digital Communications, School of Engineering, The University of Edinburgh, Edinburgh, UK, EH9 3JL (E-mail: y.yang@ed.ac.uk).

L. Ai and S. Zhang are with the Peking University Shenzhen Hospital, Shenzhen, China, 518036.

Manuscript received xx, 2021.

study aim to improve mf-EIT imaging quality by learning the non-linear relationship between the measurement data and multi-frequency conductivity distributions, with a specific focus on cell imaging applications.

Our previous work focused on data-driven approaches for cell culture imaging with EIT. We established a mono-frequency EIT dataset for image reconstruction and proposed a hybrid learning-based approach DL-GS [26], and a pure learning-based approach SADB-Net [27], for cell culture imaging. Concerning mfEIT, we in [23] constructed the *Edinburgh mfEIT Dataset* and developed the aforementioned model-based learning approach, MMV-Net, built upon the linearized mfEIT model. All these approaches were validated by experiments on MCF-7 human breast cancer cell aggregates. Based on the previous work, we here report an mfEIT image reconstruction algorithm for cell culture imaging based on the graph neural network to predict simultaneously multiple conductivity images at different frequencies directly from the mfEIT measurement data with the assistance of auxiliary images. We employ an undirected graph to represent the regular EIT grid in a non-Euclidean space (see Fig. 1). Graph nodes correspond to pixels in the regular grid and contain the corresponding conductivity values. We then propose a Mask-guided Spatial-Temporal Graph Neural Network (M-STGNN) to generate high-quality and robust mfEIT images. The general network architecture of M-STGNN is developed based on the GraphWaveNet proposed by [42]. GraphWaveNet makes predictions on multiple future steps at the same time given historical steps in traffic forecasting. Due to similar objectives, the general structure of GraphWaveNet is inherited by M-STGNN for the mfEIT-image-reconstruction problem. The key idea is to explicitly exploit both spatial and frequency correlations of mfEIT images reconstructed from the one-step Gaussian Newton solver. Learning these correlations helps fine-tune multi-frequency images. Moreover, we introduce external geometric structures from the auxiliary imaging modality in the format of binary masks to further help optimize the structural information. The geometric structure could be obtained from different imaging modalities, such as CT scans [28] and microscopic images [29]. The main contributions of this work are as follows:

1) A customized graph neural network is proposed for mfEIT image reconstruction to achieve high-quality cell culture imaging. The proposed M-STGNN is designed to approximate the non-linear relationship between measurement data and multi-frequency conductivity distributions.
2) The proposed M-STGNN incorporates spatial and frequency correlations between mfEIT images. It further utilizes external geometric structures to constrain the structural information so that the spatial correlation is learned from training data as well as this prior knowledge. This extra step is capable of stabilizing the solutions of mfEIT.
3) Both numerical analysis and real-world experiments on MCF-7 breast cancer cell demonstrate the superiority of the proposed M-STGNN in reconstructing multi-frequency images in terms of reconstruction accuracy, noise robustness, generalization ability and computational efficiency compared to the state of the art.

The remainder of this paper is organized as follows. Section II reviews related work on mfEIT image reconstruction and graph neural networks. Section III elaborates the proposed mask-guided spatial-temporal graph neural network. Section IV describes the mfEIT dataset, experimental implementation and results. Section V draws conclusion and discusses the future work.

II. Related Work

A. Multi-frequency Electrical Impedance Tomography

The EIT forward problem is defined as the calculation of the boundary voltages $\mathbf{V}$, given the conductivity distribution $\boldsymbol{\sigma}$. Let Ω denote the ROI, N be the number of electrodes attached at the boundary $\partial\Omega$, and $\mathbf{n}$ be the outward unit normal of $\partial\Omega$. We use the Complete Electrode Model (CEM) [30] to formulate the forward problem:

$$\nabla \cdot (\boldsymbol{\sigma}(x)\nabla \mathbf{u}(x)) = 0, \quad x \in \Omega \tag{1}$$

$$\mathbf{u}(x) + z_\ell \boldsymbol{\sigma}(x)\frac{\partial \mathbf{u}(x)}{\partial \mathbf{n}} = V_\ell, \quad x \in e_\ell, \ell = 1, \ldots, N \tag{2}$$

$$\int_{e_\ell} \boldsymbol{\sigma}(x)\frac{\partial \mathbf{u}(x)}{\partial \mathbf{n}} dS = I_\ell, \quad x \in e_\ell, \ell = 1, \ldots, N \tag{3}$$

$$\boldsymbol{\sigma}(x)\frac{\partial \mathbf{u}(x)}{\partial \mathbf{n}} = 0, \quad x \in \partial\Omega \backslash \cup_{\ell=1}^{N} e_\ell \tag{4}$$

where e_ℓ is the ℓth electrode; z_ℓ, I_ℓ, and V_ℓ denote respectively the contact impedance, injected currents and corresponding voltages on e_ℓ. Currents I_ℓ satisfy the conservation of charge defined by

$$\sum_{\ell=1}^{N} I_\ell = 0 \tag{5}$$

and to further stabilize the solution, we also require the convention defined by

$$\sum_{\ell=1}^{N} V_\ell = 0. \tag{6}$$

In mfEIT, current comprising a set of frequency elements $\{f_1, f_2, \ldots, f_l\}$ is injected into the ROI. The mfEIT-image-reconstruction problem is to recover the spectroscopic conductivity distributions simultaneously given boundary voltage measurements under multiple frequencies. We consider time-difference multi-frequency imaging, which can eliminate the common modelling errors to some extent. The multi-frequency conductivity changes $\Delta\boldsymbol{\sigma} \in \mathbb{R}^{n\times l}$ are reconstructed based on the voltage changes $\Delta\mathbf{V} \in \mathbb{R}^{m\times l}$. Many algorithms have been reported to address this ill-posed and ill-conditioned inverse problem [21], [23]–[25]. In this paper, we adopt the one-step Gaussian Newton solver $f_{os}(\cdot)$ with the Laplacian filter [17] to provide the initial guess. Despite fast computational time, the one-step approach is limited by image artifacts and low contrast. We employ a deep network $f(\cdot;\boldsymbol{\theta})$ parameterised by network weights $\boldsymbol{\theta}$ to improve the one-step reconstruction. The network parameters $\boldsymbol{\theta}$ are determined based on training data

$\mathcal{D}$ of input-target pairs $\{(\Delta\mathbf{V}^{(k)}, \Delta\boldsymbol{\sigma}_{gt}^{(k)})\}_{k=1}^{K}$, where $\{\Delta\boldsymbol{\sigma}_{gt}^{(k)}\}$ represents the ground truth of conductivity distributions. The inverse problem is then converted to a regression problem by minimising an objective function $\mathcal{L}$:

$$\min_{\boldsymbol{\theta}} \mathcal{L}(\boldsymbol{\theta}; \mathcal{D}) := \frac{1}{2} \sum_{(\Delta\mathbf{V}, \Delta\boldsymbol{\sigma}_{gt}) \in \mathcal{D}} \|\Delta\boldsymbol{\sigma}_{gt} - f(f_{os}(\Delta\mathbf{V}); \boldsymbol{\theta})\|^2 . \tag{7}$$

B. Graph Neural Networks

Many machine learning tasks, such as object detection, speech recognition, and machine translation, have benefited from the success of deep learning [31]–[33]. Deep learning can effectively extract latent representations of Euclidean data, which is a special case of graphs with instances assumed to be independent of each other. To generalize deep learning approaches to graph-structured data, Graph Neural Networks (GNNs) have been proposed and applied in many areas, such as molecular fingerprints [34], recommender system [35], and traffic forecasting [36]. A recent work [37] employed graph structures to construct the finite element mesh and proposed a GNN to solve the mono-frequency EIT inverse problem. Our work extends the GNN to solve the mfEIT image reconstruction problem with the assistance of auxiliary structural information.

Wu *et al.* [38] provided a comprehensive overview of GNNs, which are categorized into recurrent GNNs (RecGNNs), convolutional GNNs (ConvGNNs), graph autoencoders (GAEs), and spatial-temporal GNNs (STGNNs). Early studies in RecGNNs learned node representations by propagating messages with neighbours iteratively until a fixed point is reached. The idea of message passing of RecGNNs as well as Convolutional Neural Networks (CNNs) in computer vision motivated the development of convolution for graph data, which computes the average of neighbourhood information. ConvGNNs, as the most prominent variant GNN, consist of multiple graph convolutional layers to learn latent representations. Like autoencoders in deep learning, GAEs encode inputs into a latent space and then decode latent representations back to graph information, which is typically used for network embedding and graph generation. STGNN is a GNN variant that learns patterns from dynamic graphs by simultaneously considering spatial and temporal dependencies.

C. Spatial-temporal Graph Neural Networks

Spatial-temporal graphs are dynamic on account of node or edge features varying over time [38]. Recent state-of-art STGNN models capture spatial dependence with graph convolutions or attentions and temporal dependence with RNNs, CNNs or attentions, leading to three types of STGNNs: RNN-based, CNN-based and attention-based [39].

DCRNN [40] is an autoencoder-like RNN-based model incorporating a diffusion graph convolution network into a Gated Recurrent Unit (GRU) network. The computational problem is the main drawback of RNN-based models caused by the usage of recurrent units. CNN-based approaches [41], [42] address the problem in a non-recursively by stacking

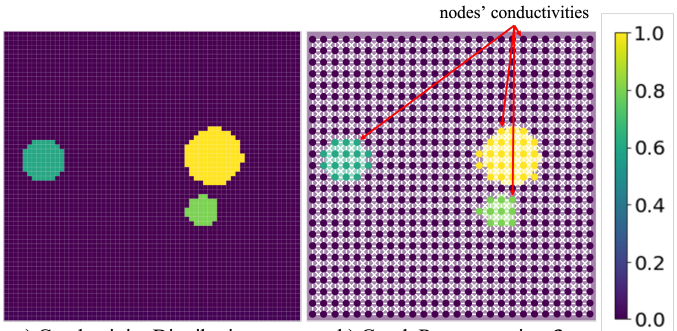

a) Conductivity Distribution on a regular grid

b) Graph Representation $\mathcal{G}$

Fig. 1. Left: conductivity distribution in Euclidean space. Right: graph representation $\mathcal{G}$ in non-Euclidean space.

multiple spatial-temporal blocks. In particular, each block of STGCN [41] includes two gated 1-D convolutional layers with a graph convolutional layer in-between. GraphWaveNet [42] utilizes dilated casual convolutions instead for temporal correlation based on the WaveNet proposed by [43]. This architecture is widely adopted as it provides promising results for various dynamic datasets. In the aforementioned graph convolutions, neighbor features of nodes are aggregated with equal or handcrafted weights. To avoid pre-definition and learn these weights through training, the multi-attention mechanism is introduced into STGNNs in an autoencoder architecture [44]. In this work, the proposed network is developed based on the architecture of GraphWaveNet for dynamic datasets.

III. Methodology

A. mfEIT Graph Representation

Fig. 1 shows the transformation of EIT grid from Euclidean domain to non-Euclidean domain. The undirected graph is represented as $\mathcal{G} = (\mathcal{V}, \mathcal{E})$ with n nodes $v_i \in \mathcal{V}$ and edges $(v_i, v_j) \in \mathcal{E}$. The adjacency matrix $\mathbf{A} \in \mathbb{R}^{n \times n}$ describes edges of the graph $\mathcal{G}$. If $(v_i, v_j) \in \mathcal{E}$, the intersection $\mathbf{A}_{ij}$ of the ith row and the jth column is determined by

$$\mathbf{A}_{ij} = e^{-\frac{(v_i - v_j)^2}{\beta^2}} \tag{8}$$

where β is a free parameter and is set as 0.05π in this paper. Otherwise, $\mathbf{A}_{ij}$ is zero. $\mathbf{A}$ is then normalized based on [45]. At each frequency channel $f \in \{f_1, f_2, \ldots, f_l\}$, the graph $\mathcal{G}$ has a dynamic node feature matrix $\mathbf{X}^f \in \mathbb{R}^{n \times 1}$, where each node v_i is assigned a single feature to represent the conductivity change.

Let $\mathbf{X}_{os}^{f_1:f_l} \in \mathbb{R}^{n \times l}$ be the low-quality reconstruction obtained from the one-step Gaussian Newton solver, and $\mathbf{M} \in \mathbb{R}^n$ be the structural constraint in hand in form of binary masks. Given a graph $\mathcal{G}$, this paper aims to learn a function g to improve the quality of $\mathbf{X}_{os}^{f_1:f_l}$ constrained by $\mathbf{M}$, which is formulated as

$$[\mathbf{X}_{os}^{f_1:f_l}, \mathbf{M}, \mathcal{G}] \xrightarrow{g} \mathbf{X}_{M-STGNN}^{f_1:f_l} \tag{9}$$

where $\mathbf{X}_{M-STGNN}^{f_1:f_l} \in \mathbb{R}^{n \times l}$ stands for the enhanced reconstruction by the proposed Mask-guided Spatial-Temporal

Graph Neural Network, which will be discussed in Section III-B.

B. Mask-guided Spatial-Temporal Graph Neural Network

Images reconstructed from the one-step Gaussian Newton solver suffer from high sensitivity to noise, blurriness and artifacts. We hypothesize that explicitly learning spatial and frequency correlations of these mfEIT images could improve the image quality. We propose to constrain the spatial correlation by binary masks available to optimize the structural information. The binary masks could be extracted from, for instance, CT scans [28] and microscopic images in the same ROI using a multi-modal imaging setup [29]. Thereafter, a Mask-guided STGNN network (M-STGNN) (see Fig. 2) is proposed to achieve high-quality mfEIT images. The network architecture of M-STGNN is similar to GraphWaveNet [42]. GraphWaveNet was originally designed for traffic forecasting. Given multiple historical steps, GraphWaveNet predicts multiple future steps as a whole rather than in a recursive way. Its framework is capable of capturing spatial-temporal dependencies simultaneously. We argue that the general architecture of GraphWaveNet is appropriate for mfEIT image reconstruction due to similar objectives.

Fig. 2 presents the framework of M-STGNN comprising of input and output layers, and a stack of ST-GCN layers. Each ST-GCN layer has a graph convolution layer (GCN) and a gated temporal convolution layer (GTCN), which is constructed by two parallel dilated convolution layers. The ST-GCN layers also apply residual connection and are skip-connected to the output layers. The last ST-GCN layer reduces the frequency dimension to one. For the following linear layers, the output channel number of each layer is a factor of frequency channels l.

The key idea of this architecture is to learn spatial and frequency dependencies by GCNs and GTCNs respectively. In terms of the spatial dependency, M-STGNN relies on not only the learning process of GCNs but also the prior knowledge from structural constraint $\mathbf{M}$. Therefore, both input $\mathbf{H}^{(k-1)} \in \mathbb{R}^{n\times c}$ and $\mathbf{M}$ are fed into the kth GCN. Let $\mathbf{Z}^{(k)} \in \mathbb{R}^{n\times d}$ be the output, and $\mathbf{W} \in \mathbb{R}^{c\times d}$ be the network weights, the GCN adopts a diffusion process with T finite steps, which is defined as

$$\mathbf{Z}^{(k)} = \sum_{t=0}^{T} \frac{\mathbf{A}^t}{rowsum(\mathbf{A}^t)}(\mathbf{H}^{(k-1)} \odot \mathbf{M})\mathbf{W}_{t1} + \mathbf{A}_{apt}^t(\mathbf{H}^{(k-1)} \odot \mathbf{M})\mathbf{W}_{t2} \tag{10}$$

where $\mathbf{A}_{apt}$ denotes the self-adaptive adjacency matrix proposed in [42] to learn hidden spatial dependency, and $\odot$ denotes element-wise product. $\mathbf{Z}^{(k)}$ is then passed to the GTCN to capture the trend of each node along frequency. The GTCN employs two parallel dilated casual convolution layers followed by different activation layers. 1-D dilated casual convolution [46] slides over the input along the frequency dimension by a skipping distance with a certain step. By stacking ST-GCN layers with increasing the skipping distance for GTCNs, the receptive field of the network is enlarged to capture longer-term dependency. In other words, early stage ST-GCN learns short-term frequency correlation whereas the last ST-GCN learns long-term frequency correlation.

Compared to GraphWaveNet, several modifications have been made in M-STGNN, which are listed as follows:

1) The binary mask $\mathbf{M}$ is introduced to GCNs to constrain the structural information in a way that spatial correlation benefits from both prior knowledge and training data.
2) Our previous work [26] on mono-frequency EIT imaging observed that structural information of the conductivity image enables significant image quality improvement. M-STGNN inherits this idea by swapping the sequence of GTCNs and GCNs of GraphWaveNet.
3) GraphWaveNet treats all nodes as a whole in terms of temporal correlation, indicating that all nodes in a graph share the same temporal trend. This property is unsuitable for mfEIT imaging, where different objects possess different frequency correlations. Instead, M-STGNN assigns independent learning kernels for all nodes.

TABLE I
SAMPLE NUMBERS IN EACH DATA SET

Dataset	*Training*	*Validation*	*Testing*
Before Augmentation	$4 \times 8,700$	$4 \times 1,900$	$4 \times 1,814$
After Augmentation	$4 \times 13,050$	$4 \times 2,850$	$4 \times 5,442$

IV. EXPERIMENTS AND RESULTS

A. Dataset

We verify M-STGNN on the *Edinburgh mfEIT Dataset* constructed by the authors [23]. The dataset is constructed by simulation using COMSOL Multiphysics and MATLAB, which is available at: https://datashare.ed.ac.uk/handle/10283/4441. It contains $4 \times 12,414$ voltage measurements and conductivity pairs at four distinct frequencies. We adopt the same data normalization as in [23]. The dataset is then split into training ($4 \times 8,700$ samples: $4 \times 2,100$ samples of one-object pattern, $4 \times 2,800$ samples of two-object pattern, and $4 \times 3,800$ samples of three-object pattern), validation ($4 \times 1,900$ samples: 4×500 samples of one-object pattern, 4×600 samples of two-object pattern, and 4×800 samples of three-object pattern) and testing ($4 \times 1,814$ samples: 4×400 samples of one-object pattern, 4×600 samples of two-object pattern, and 4×814 samples of three-object pattern) sets. We also conduct data augmentation by adding Gaussian noise with different Signal-to-Noise Ratios (SNRs) to voltage measurements. White noise with Signal-to-Noise Ratio (SNR) of 50dB is added to half samples in the training and validation set. White noise with SNR of 50dB, 40dB and 30dB is respectively added to all samples in the testing subset. Table I summarizes the data size in training, validation, and testing subsets before and after data augmentation. Corresponding binary masks for training data are generated by setting all non-zero conductivity values of true images as one.

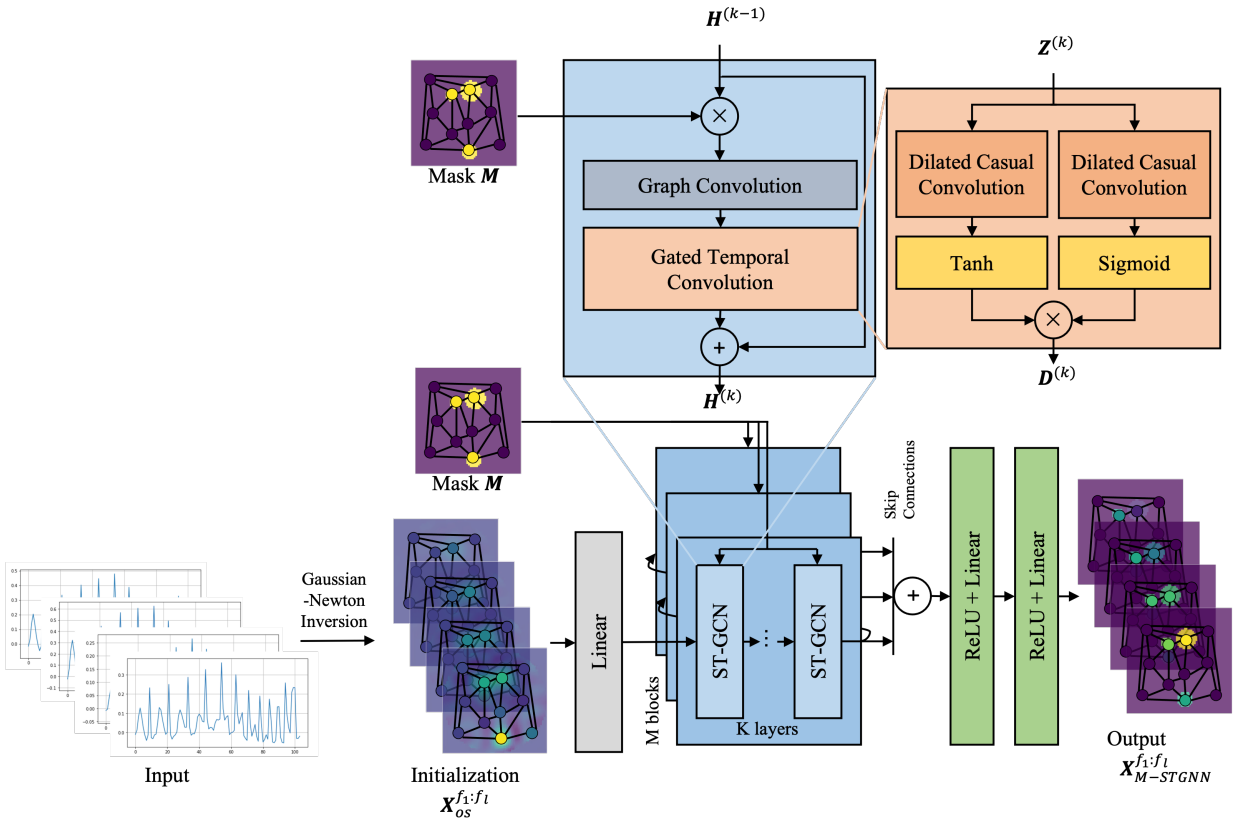

Fig. 2. Schematic illustration of Mask-guided Spatial-Temporal Graph Neural Network (M-STGNN).

B. Network Training

We train the M-STGNN using PyTorch. The Mean Square Error (MSE) is selected as the loss function. We use Adam [47] for optimization with a batch size of 20 and a weight decay of 5e-6. The learning rate starts at 0.0001 and is decreased by a factor of 0.1 with a step size of 20. The maximum training epoch is 200.

C. Baselines

We compare M-STGNN with several state-of-the-art mfEIT image reconstruction approaches:

- MMV-ADMM [22] is a traditional iterative algorithm which was reported for multi-frequency complex electrical capacitance tomography but can also be applied for mfEIT image reconstruction. The maximum iteration number is set as 100.
- MMV-Net [23] is a model-based deep learning method proposed by the authors that unrolls the MMV-ADMM algorithm for mfEIT image reconstruction. We adopt the same training procedure as in [23].
- GraphWaveNet [42] is a spatial-temporal graph neural network which incorporates graph convolution and dilated casual convolution designed for traffic forecasting. This architecture can be applied for mfEIT image reconstruction due to the similar property of dynamic datasets. The training procedure is the same as that for M-STGNN.

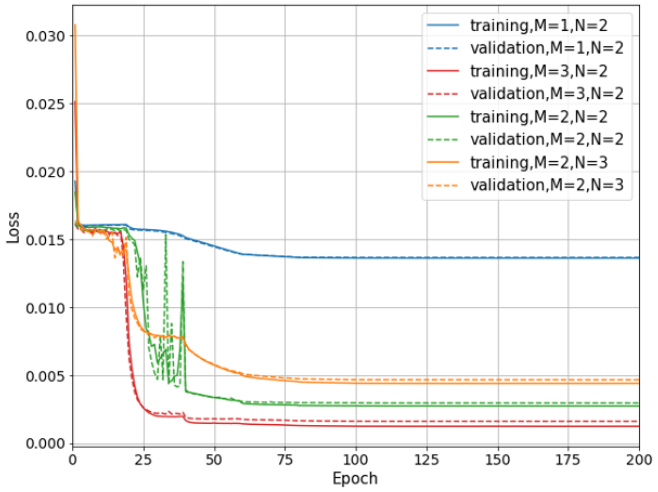

Fig. 3. The learning curves illustrate the variation among different choices of the block number M and the layer number N.

D. Evaluation on Simulation Data

1) Learning Curves: Learning curves in Fig. 3 show the impact of different choices of the block number M and the layer number N. The red lines drop faster at the early stage and generates the lowest asymptote. This implies that the model with M=3 and K=2 can learn faster and eventually provide the best validation performance.

TABLE II
PERFORMANCE COMPARISONS (PSNR, SSIM, RMSE AND FPS) ON EDINBURGH MFEIT DATASET. FPS MEANS FRAME PER SECOND

Metrics	*SNR (dB)*	MMV-ADMM [22]	MMV-Net [23]	Graph-WaveNet [42]	M-STGNN
PSNR	*Noise Free*	23.0880	26.7585	25.8098	**29.2829**
	50	22.9291	25.4704	24.1782	**29.2824**
	40	22.7070	23.0531	19.5365	**29.2820**
	30	21.5629	21.6358	13.6622	**29.2797**
SSIM	*Noise Free*	0.5543	0.9350	0.9137	**0.9693**
	50	0.5385	0.8855	0.8464	**0.9693**
	40	0.5238	0.8143	0.6064	**0.9693**
	30	0.4877	0.6842	0.3304	**0.9693**
RMSE	*Noise Free*	0.0803	0.0510	0.0578	**0.0378**
	50	0.0809	0.0602	0.0715	**0.0378**
	40	0.0822	0.0807	0.1320	**0.0378**
	30	0.0989	0.0904	0.2535	**0.0378**
No. of learning parameters		NA	8,780	85,676	503,472,290
FPS (ft/s)		1.39	7.92	**97.71**	**24.73**

Best results are highlighted in bold.

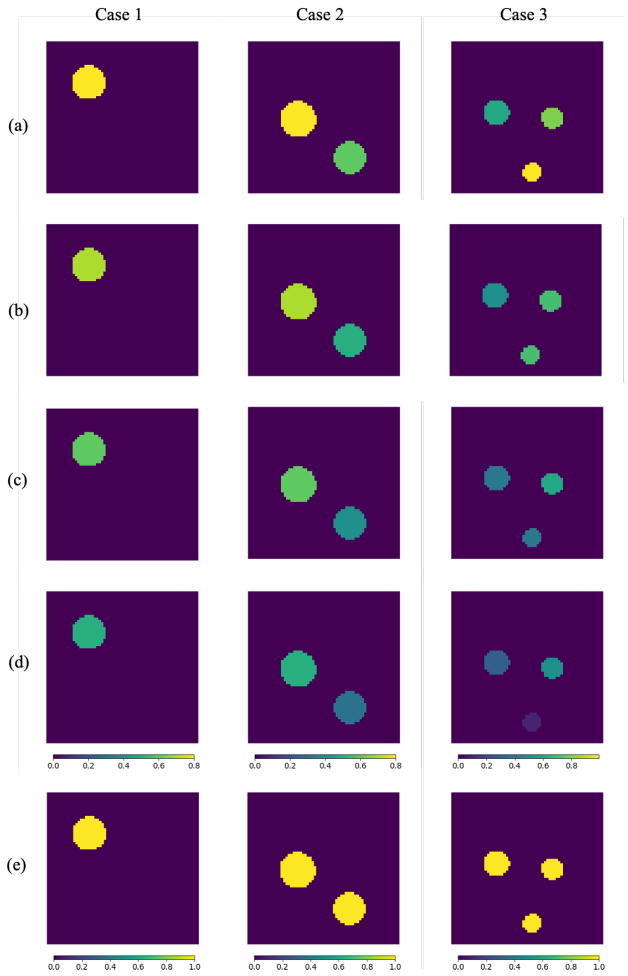

Fig. 4. Three different cases from the testing set. (a)-(d) Truth conductivity distributions at f_1, f_2, f_3, and f_4. (e) Corresponding binary masks.

2) Quantitative Comparisons: Table II reports quantitative comparisons based on average Peak Signal to Noise Ratio (PSNR), Structural Similarity Index Measure (SSIM), and Root Mean Square Error (RMSE) over all the testing data. M-STGNN consistently outperforms all competing approaches on all metrics. To further evaluate the robustness against noise, we add different levels of Gaussian noise to the measurement data, i.e., noise free, 50dB, 40dB, and 30dB. MMV-ADMM, MMV-Net, and GraphWaveNet show a clear trend of degrading performance with decreasing SNR. In contrast, M-STGNN exhibits overwhelming noise robustness performance, which reveals the effectiveness of the structural constraint from external binary masks.

We also compare the running speed of all algorithms. All learning-based approaches run much faster than MMV-ADMM while obtaining higher image quality, suitable for real-time mfEIT imaging. GraphWaveNet and M-STGNN are respectively 12.3 times and 3.1 times faster than MMV-Net, indicating the superiority of GNNs over model-based learning approaches. M-STGNN runs slower than GraphWaveNet by 73.18 ft/s. The main reason is that the trainable parameters of M-STGNN is about 2k times larger than GraphWaveNet (see the last second row in Table II) because it uses independent parameters to learn temporal correlations for each node and an extra branch to deal with the binary masks. Thus the average inference speed of M-STGNN increases compared to GraphWaveNet. Nevertheless, M-STGNN can achieve 24.73 ft/s, which is still sufficient for real-time mfEIT imaging.

3) Case Study: Three representative cases with different patterns are selected from the testing set when SNR is 50dB (see Fig. 4).

Fig. 5 shows corresponding mfEIT reconstruction results of all algorithms. Overall, M-STGNN outperforms the other three algorithms under all frequencies visually and quantitatively, whereas MMV-ADMM keeps suffering from low resolution and blurriness. In case 1, all algorithms are capable of recovering the object shape and the trend of conductivity variation along the frequency. The case 2 is more challenging with two inclusions of different conductivity, which MMV-ADMM hardly separates. MMV-Net is unable to reconstruct the shape of the lower right inclusion accurately. Graph-WaveNet performs even worse with distorted shape of both inclusions, whereas M-STGNN provides the most accurate shape, constrained by the binary masks. Regarding case 3, MMV-ADMM is unable to distinguish the two inclusions at the top and even fails to recognize the top-left inclusion at f_4. All learning-based approaches outperform MMV-ADMM, especially in terms of shape reconstruction.

It is noteworthy that ideally we expect M-STGNN to generate accurate conductivity estimation for all objects, especially with the structural information constrained by the binary masks. However, when there are multiple inclusions within the ROI with different conductivity, what M-STGNN learns from the training data is to assign similar conductivity values to all inclusions, which is similar to the results of MMV-Net and GraphWaveNet. The potential reason could be that the capability to distinguish multi-level conductivity is limited by the information provided by the current EIT sensor

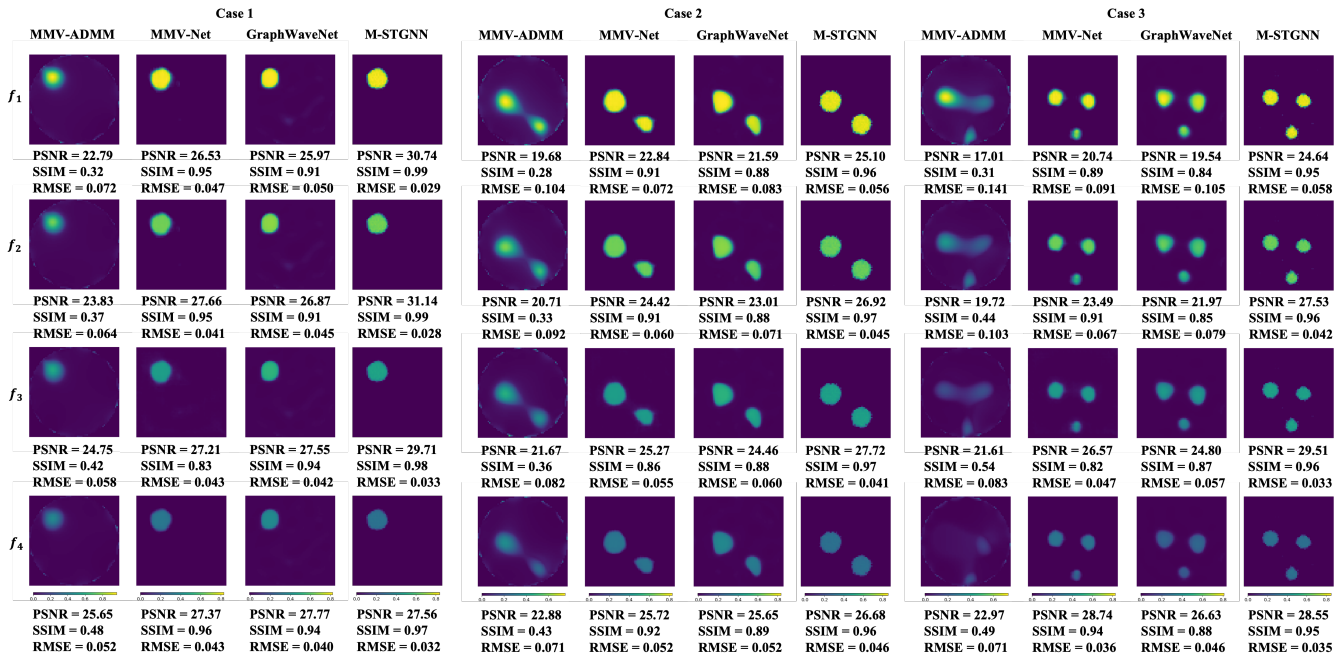

Fig. 5. Reconstructed results of M-STGNN compared to baseline approaches when SNR is 50dB.

TABLE III
NUMERICAL COMPARISONS OF EXPERIMENTAL RESULTS BASED ON SSIM.

Metrics	*Frequency* (kHz)	MMV-ADMM [22]	MMV-Net [23]	Graph-WaveNet [42]	M-STGNN
1	50	0.7355	0.8530	0.8353	**0.9665**
	40	0.7116	0.8540	0.8429	**0.9523**
	30	0.6284	0.8505	0.8312	**0.9261**
	20	0.6955	0.8454	0.8411	**0.8904**
2	50	0.7617	0.8184	0.8462	**0.9684**
	40	0.6661	0.8292	0.8401	**0.9541**
	30	0.6208	0.8352	0.8383	**0.9275**
	20	0.7262	0.8466	0.8428	**0.9471**
3	50	0.7154	0.8487	0.8352	**0.9734**
	40	0.7403	0.8501	0.8428	**0.9579**
	30	0.6626	0.8496	0.8365	**0.9311**
	20	0.7474	0.8552	0.8475	**0.8955**
4	100	0.2716	0.8574	0.7266	**0.9695**
	80	0.3964	0.8566	0.7421	**0.9558**
	50	0.3390	0.8523	0.7575	**0.9332**
	40	0.3588	0.8502	0.7950	**0.9038**

Best results are highlighted in bold.

layout, which might be solved by deploying more electrodes (e.g., at the substrate of the sensor) in order to obtain more measurements.

E. Evaluation on Experimental Data

In addition to simulation study, we carried out real-world experiments on human breast cancer cell spheroids with a quasi-2-D miniature EIT sensor [48] to examine the generalization ability of the proposed method. The sensor with a diameter of 14 mm is equipped with 16 planar electrodes (see Fig. 6). The imaging targets are 3D cultivated MCF-7 cell (e.g., cells cultivated in a 3D format to better mimic tissues, such as spheroids and scaffolds) in the laboratory environment. The background substance is the standard Dulbecco's Modified Eagle's Medium for cell culture with a conductivity of 2 $S \cdot m^{-1}$ (Life Technologies, Carlsbad, CA, USA) [14]. All MCF-7 human breast cancer cell spheroids are less conductive than the background substance at the frequencies of interest. The conductivity of MCF-7 human breast cancer cell spheroids will increase with the increasing current frequency. The circular cell spheroids in Fig. 6 (b), (d), and (f) have a diameter of around 2 mm [26], [27]. In these cases, the excitation frequencies are $\{f_1, f_2, f_3, f_4\} = \{50, 40, 30, 20\}kHz$. The experiment on the triangular MCF-7 human breast cancer cell pellet in Fig. 6 (g) refers to our previous work in [23], where the excitation frequencies are $\{f_1, f_2, f_3, f_4\} = \{100, 80, 50, 40\}kHz$. The binary masks in Fig. 6 (b), (d), (f) and (h) are extracted according to the microscopic images in Fig. 6 (a), (c), (e) and (g). The experimental data are not guaranteed to have the same impedance spectra as the simulation data because we focus more on capturing the frequency correlation of conductivity values. However, the simulation data can cover the possible conductivity variation range caused by MCF-7 cells.

Fig. 7 illustrates the mfEIT image reconstruction results of the four experimental phantoms. Additionally, Table III reports the quantitative comparisons of corresponding results based on SSIM. Overall, MMV-ADMM fails to, but the three learning-based approaches manage to consistently provide a clear trend of conductivity changes along frequency. Among them, M-STGNN achieves significantly better shape reconstruction. For phantom 1, MMV-ADMM generates evident artifacts at lower frequencies. MMV-Net and GraphWaveNet underestimate the size of both cell spheroids. M-STGNN provides the better shapes under all frequencies. The two cell spheroids get closer in phantom 2. Both MMV-ADMM and MMV-Net exhibit

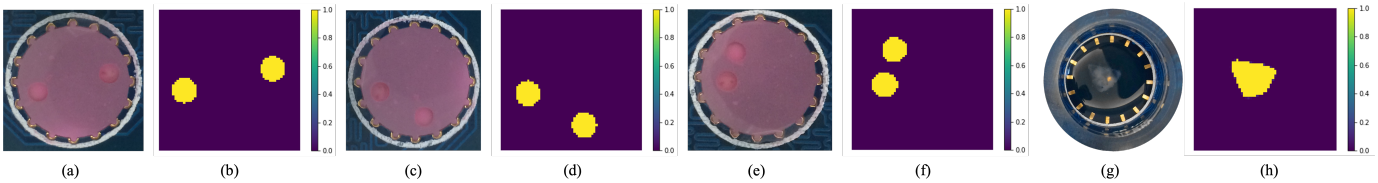

Fig. 6. Experimental phantoms on 16-electrode miniature EIT sensor. (a) Phantom 1: two MCF-7 cell spheroids [27]. (b) Binary mask of phantom 1. (c) Phantom 2: two MCF-7 cell spheroids [26]. (d) Binary mask of phantom 2. (e) Phantom 3: two MCF-7 cell spheroids [26]. (f) Binary mask of phantom 3. (g) Phantom 4: a MCF-7 cell spheroid [23]. (h) Binary mask of phantom 4.

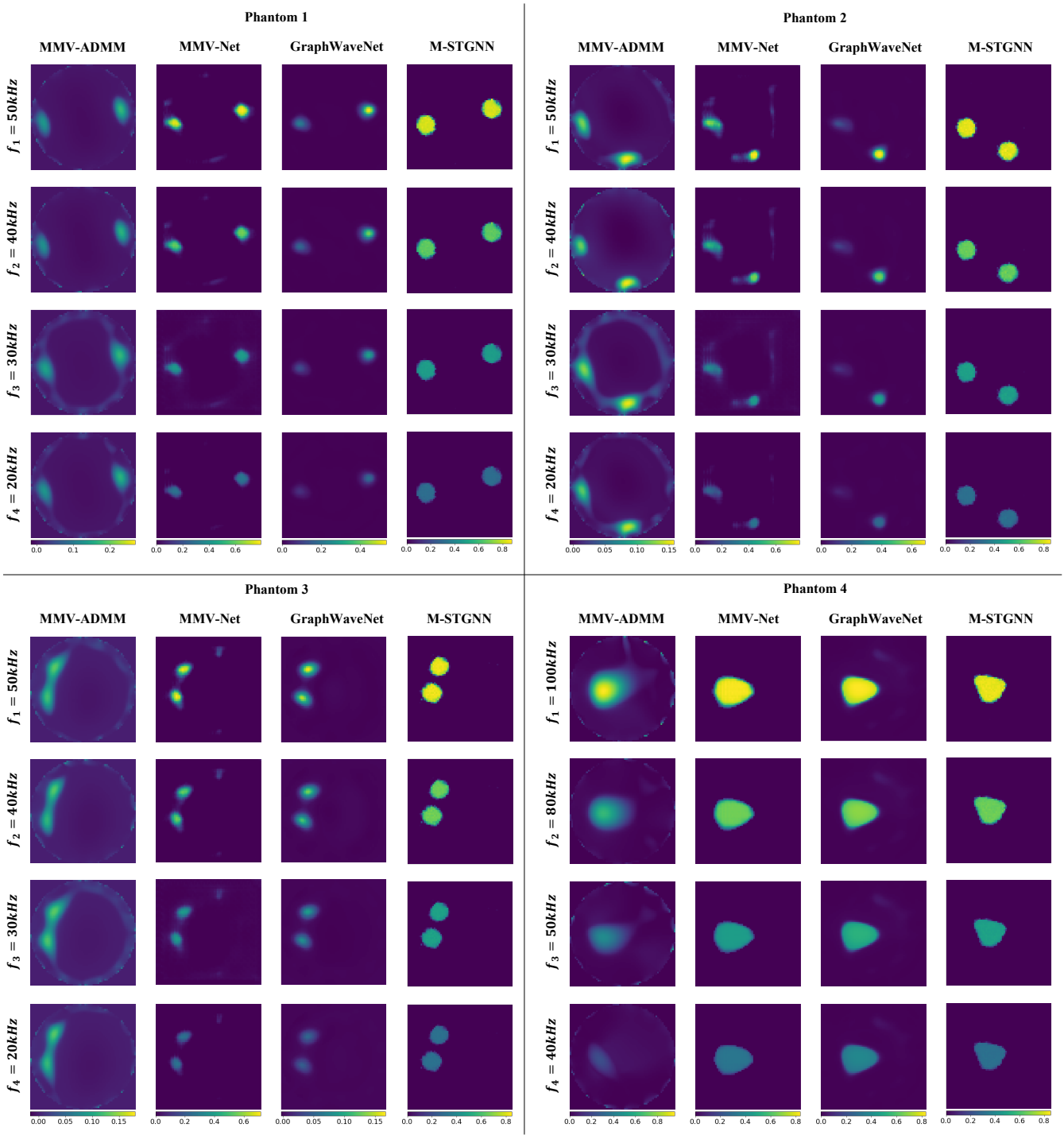

Fig. 7. Reconstructed results of four experimental phantoms.

poor ability in terms of noise reduction. GraphWaveNet could only roughly recover the cell spheroid on the left while M-STGNN demonstrates superior performance in terms of both shape preservation and noise reduction. For phantom 3, MMV-ADMM is unable to distinguish the two adjacent cell spheroids. MMV-Net and GraphWaveNet manage to separate them but their sizes are underestimated. However, M-STGNN consistently yields better shapes at all frequencies. Phantom 4 is a simpler scenario with a single cell spheroid. MMV-ADMM reconstructs the trend of conductivity changes along frequency but with distorted shapes. The three learning-based approaches are able to provide the unseen triangular shape whereas M-STGNN is more powerful in shape preservation, which mainly benefits from the strong structural constrain from the binary mask.

The results suggest that M-STGNN generalizes well to real-world experiments on MCF-7 human breast cancer cell spheroids. It outperforms the conventional iterative algorithm and the state-of-the-art learning-based approaches by learning both spatial and frequency correlations of mfEIT images and exploiting external binary masks to constrain the general structures.

V. Conclusion

This study proposes a novel graph neural network M-STGNN to address the image reconstruction problem of mfEIT, with a particular focus on tissue engineering applications. M-STGNN learns both spatial and frequency correlations between mfEIT images. Additionally, M-STGNN considers the multi-modal imaging context and introduces binary masks from auxiliary imaging modalities such as optical imaging to constrain the fine structure of mfEIT images. Simulations and real-world experiments are conducted to evaluate and benchmark the performance of M-STGNN quantitatively. The results show that M-STGNN can achieve considerable improvements in shape preservation and noise robustness, compared to the state-of-the-art mfEIT image reconstruction approaches. In the future work, we aim to extend this approach to optical-mfEIT dual-modal imaging to screen the dynamic 3D cell activities (e.g., cell-drug response) in real time. The main challenges for extending to 3D setup lie in a few aspects, e.g., the acquisition and processing of 3D masks, the construction of 3D training dataset, and the higher-dimension inverse problem.

References

[1] E. Malone, G. S. dos Santos, and D. S. Holder, "Multifrequency electrical impedance tomography using spectral constraints," *IEEE Trans. Med. Imag.,* vol. 33, no. 2, pp. 340–350, Feb. 2014.

[2] M. Goharian et al., "A DSP based multi-frequency 3D electrical impedance tomography system," *Ann. Biomed. Eng.,* vol. 36, no. 9, pp. 1594–1603, Feb. 2008.

[3] Y. Yang and J. Jia, "A multi-frequency electrical impedance tomography system for real-time 2D and 3D imaging," Rev. Sci. Instrum., vol. 88, p. 085110, Aug. 2017.

[4] R. H. Bayford, "Bioimpedance tomography (electrical impedance tomography)," *Annu. Rev. Biomed. Eng.*, vol. 8, pp. 63–91, Aug. 2006.

[5] A. Adler and A. Boyle, "Electrical impedance tomography: Tissue properties to image measures," *IEEE Trans. Biomed. Eng.,* vol. 64, no. 11, pp. 2494–2504, Nov. 2017.

[6] L. Yang, C. Xu, M. Dai, F. Fu, X. Shi, and X. Dong, "A novel multi-frequency electrical impedance tomography spectral imaging algorithm for early stroke detection," *Physiol. Meas.,* vol. 37, no. 12, pp. 2317–2335, Nov. 2016.

[7] B. Packham et al., "Comparison of frequency difference reconstruction algorithms for the detection of acute stroke using EIT in a realistic headshaped tank," *Physiol. Meas.,* vol. 33, pp. 767–786, 2012.

[8] Y. Zhou, and X. Li. "Multifrequency time difference EIT imaging of cardiac activities," *Biomed. Signal Proces.,* vol. 38, pp: 128-135, 2017.

[9] T. I. Oh, J. Lee, J. K. Seo, S. W. Kim, and E. J. Woo, "Feasibility of breast cancer lesion detection using a multifrequency trans-admittance scanner (TAS) with 10 Hz to 500 kHz bandwidth," *Physiol. Meas.,* vol. 28, pp. S71–S84, 2007.

[10] E. Lee, M.-E. Ts, J. K. Seo, and E. J. Woo, "Breast EIT using a new projected image reconstruction method with multi-frequency measurements," *Physiol. Meas.,* vol. 33, pp. 751–765, Apr. 2012.

[11] J. Kuen, E. J. Woo, and J. K. Seo, "Multi-frequency time-difference complex conductivity imaging of canine and human lungs using the KHU Mark1 EIT system," *Physiol. Meas.,* vol. 30, pp. S149–S164, 2009.

[12] S. A. Santos et al., "Lung pathologies analyzed with multi-frequency electrical impedance tomography: Pilot animal study," *Respir. Physiol. Neurobiol.,* vol. 254, pp. 1–9, Aug. 2018.

[13] H. Wu, Y. Yang, P. O. Bagnaninchi, and J. Jia, "Imaging cell-drug response in 3D bioscaffolds by electrical impedance tomography," in *2017 IEEE International Conference on Imaging Systems and Techniques (IST),* (pp. 1–5). https://doi.org/10.1109/IST.2017.8261511

[14] H. Wu, W. Zhou, Y. Yang, J. Jia, and P. O. Bagnaninchi, "Exploring the potential of electrical impedance tomography for tissue engineering applications," *Materials,* vol. 11, no. 6, pp. 930, May 2018.

[15] Y. Yang, J. Jia, S. Smith, N. Jamil, W. Gamal, and P. O. Bagnaninchi, "A miniature electrical impedance tomography sensor and 3-D image reconstruction for cell imaging," *IEEE Sensors J.*, vol. 17, no. 2, pp. 514—523, Jan. 2017.

[16] Y. Yang, H. Wu, J. Jia, P. O. Bagnaninchi, "Scaffold-based 3-D Cell Culture Imaging Using a Miniature Electrical Impedance Tomography Sensor." *IEEE Sensors J.*, vol. 19, no. 20, pp. 9071—9080, Jun. 2019.

[17] A. Adler et al., "GREIT: A unified approach to 2D linear EIT reconstruction of lung images," *Physiol. Meas.,* vol. 30, pp. S35–S55, 2009.

[18] A. Borsic, B. M. Graham, A. Adler, and W. Lionheart, "In vivo impedance imaging with total variation regularization," *IEEE Trans. Med. Imag.*, vol. 29, no. 1, pp. 44–54, Jan. 2010.

[19] B. Jin, T. Khan, and P. Maass, "A reconstruction algorithm for electrical impedance tomography based on sparsity regularization," *Int. J. Numer. Methods Eng.*, vol. 89, no. 3, pp. 337–353, 2012.

[20] J. Ziniel and P. Schniter, "Efficient high-dimensional inference in the multiple measurement vector problem," *IEEE Trans. Signal Process.,* vol. 61, no. 2, pp. 340–354, 2012.

[21] G. S. Alberti et al., "The linearized inverse problem in multifrequency electrical impedance tomography," *SIAM J. Imag. Sci.,* vol. 9, no. 4, pp. 1525–1551, Apr. 2016.

[22] M. Zhang, L. Zhu, H. Wang, M. Soleimani, and Y. Yang, "Multiple Measurement Vector Based Complex-Valued Multi-Frequency ECT," *IEEE Trans. Instrum. Meas.,* vol. 70, 2021.

[23] Z. Chen, J. Xiang, Y. Yang, and P. Bagnaninchi, "MMV-Net: A Multiple Measurement Vector Network for Multi-frequency Electrical Impedance Tomography," arXiv preprint arXiv:2105.12474.

[24] S. Liu, Y. Huang, H. Wu, C. Tan, and J. Jia, "Efficient multitask structure-aware sparse Bayesian learning for frequency-difference electrical impedance tomography," *IEEE Trans. Ind. Informat.,* vol. 17, no. 1, 2021.

[25] J. Xiang, Y. Dong, and Y. Yang, "Multi-Frequency Electromagnetic Tomography for Acute Stroke Detection Using Frequency-Constrained Sparse Bayesian Learning," *IEEE Trans. Med. Imag.,* vol. 39, no. 21, 2020.

[26] Z. Chen, Y. Yang, and P. Bagnaninchi, "Hybrid Learning based Cell Aggregate Imaging with Miniature Electrical Impedance Tomography," *IEEE Trans. Instrum. Meas.,* vol. 70, 2021.

[27] Z. Chen, and Y. Yang, "Structure-Aware Dual-Branch Network for Electrical Impedance Tomography in Cell Culture Imaging," *IEEE Trans. Instrum. Meas.,* vol. 70, 2021.

[28] Z. Li, J. Zhang, D. Liu, and J. Du, "CT Image-Guided Electrical Impedance Tomography for Medical Imaging," *IEEE Trans. Med. Imag.,* vol. 39, no. 6, pp. 1822–1832, 2020.

[29] Z. Liu, P. Bagnaninchi, and Y. Yang, "Impedance-optical Dual-modal Cell Culture Imaging with Learning-based Information Fusion," *IEEE Trans. Med. Imag.,* 2021, DOI 10.1109/TMI.2021.3129739.

[30] K. S. Cheng, D. Isaacson, J. C. Newell, and D. G. Gisser, "Electrode models for electric current computed tomography," *IEEE Trans. Biomed. Eng.,* vol. 36, pp. 918–924, 1989.
[31] S. Ren, K. He, R. Girshick, and J. Sun, "Faster R-CNN: Towards real-time object detection with region proposal networks," *IEEE Trans. Pattern Anal. Mach. Intell.*, vol. 39, no. 6, pp. 1137–1149, Jun. 2017.
[32] Shiliang Zhang, Ming Lei, Zhijie Yan, and Lirong Dai, "Deep-fsmn for large vocabulary continuous speech recognition," in *ICASSP*, 2018.
[33] Y. Wu et al., "Google's neural machine translation system: Bridging the gap between human and machine translation," 2016, arXiv:1609.08144. [Online]. Available: http://arxiv.org/abs/1609.08144
[34] D. K. Duvenaud et al., "Convolutional networks on graphs for learning molecular fingerprints," in *Proc. NIPS,*2015, pp. 2224–2232.
[35] F. Monti, M. Bronstein, and X. Bresson, "Geometric matrix completion with recurrent multi-graph neural networks," in *Proc. NIPS,* 2017, pp. 3697–3707.
[36] Y. Li, R. Yu, C. Shahabi, and Y. Liu, "Diffusion convolutional recurrent neural network: Data-driven traffic forecasting," in *Proc. ICLR,* 2018, pp. 1–16.
[37] W. Herzberg, D. Rowe, A. Hauptmann, and S. Hamilton, "Graph convolutional networks for model-based learning in nonlinear inverse problems," *IEEE Trans. Comput. Imaging,* 2021, vol. 7, pp. 1341-1353..
[38] Z. Wu, S. Pan, F. Chen, G. Long, C. Zhang, and P. S. Yu, "A comprehensive survey on graph neural networks," *IEEE Trans. Neural Netw. Learn. Syst*, vol. 32, no. 1, pp. 4-24, Jan. 2021.
[39] N. Bui Khac Hoai, J. Cho, and H. Yi, "Spatial-temporal graph neural network for traffic forecasting: An overview and open research issues," *Applied Intelligence*, 06 2021.
[40] Y. Li, R. Yu, C. Shahabi, and Y. Liu, "Diffusion convolutional recurrent neural network: Data-driven traffic forecasting," in *Proc. ICLR,* 2018, pp. 1–16.
[41] B. Yu, H. Yin, and Z. Zhu, "Spatio-temporal graph convolutional networks: A deep learning framework for traffic forecasting," in *Proc. IJCAI,* Jul. 2018, pp. 3634–3640.
[42] Z. Wu, S. Pan, G. Long, J. Jiang, and C. Zhang, "Graph WaveNet for deep spatial-temporal graph modeling," in *Proc. IJCAI,* Aug. 2019, pp. 1–7.
[43] A. V. D. Oord, S. Dieleman, H. Zen, K. Simonyan, O. Vinyals, A. Graves, N. Kalchbrenner, A. Senior, and K. Kavukcuoglu, "WaveNet: A generative model for raw audio," in *Proc. Social Serv. Wheels Int. Symp. Comput. Architecture,* 2016.
[44] C. Zheng, X. Fan, C. Wang, and J. Qi, "GMAN: A graph multi-attention network for traffic prediction," in *Proc. AAAI Conf. Artif. Intell.,* 2020, pp. 1–8.
[45] T. N. Kipf and M. Welling, "Semi-supervised classification with graph convolutional networks," in *Proc. ICLR,* 2017, pp. 1–14.
[46] F. Yu and V. Koltun, "Multi-scale context aggregation by dilated convolutions," in *Proc. ICLR,* 2016.
[47] D. P. Kingma and J. L. Ba, "Adam: A method for stochastic optimization," in *Proc. Int. Conf. Learn. Represent.*, 2015, pp. 1–41.
[48] Y. Yang, H. Wu, and J. Jia, "Quasi-2D EIT-optical Dual Modality Sensor for Cellular Imaging," ELECTRICAL IMPEDANCE TOMOGRAPHY., 2018.